energy&fuels

pubs.acs.org/EF

Article

Enhancing Water Electrolysis Efficiency with NiSe@$CoSe_2$: A Superior Bifunctional Catalyst for Alkaline and Seawater Electrolytes

Yijia Cheng, Lili Sui, Xingyan Guo, Dan Yang, Shuai Du, and Lihua Miao*

Cite This: *Energy Fuels* 2026, 40, 721−729

Read Online

ACCESS | Metrics & More | Article Recommendations

ABSTRACT: Water electrolysis technology is considered one of the most promising methods for producing high-purity hydrogen and oxygen, attracting significant attention. The development of low-cost, efficient, and stable electrocatalysts for water electrolysis is crucial. In this study, we prepared a highly efficient bifunctional electrocatalyst, NiSe@$CoSe_2$, using a hydrothermal method, suitable for both alkaline and seawater electrolytes. The unique semimetallic properties of selenium contribute to the excellent catalytic performance of NiSe@$CoSe_2$. In alkaline electrolyte, at a current density of 10 mA cm^{-2}, the hydrogen evolution reaction (HER) overpotential is −153.7 mV (OER overpotential: 242.3 mV at 10 mA cm^{-2}), and the HER Tafel slope is 140.1 mV dec^{-1} (OER Tafel slope: 120.4 mV dec^{-1}). In seawater electrolyte, at a current density of 10 mA cm^{-2}, the HER overpotential is −170.7 mV (OER overpotential: 156.5 mV at 30 mA cm^{-2}), with the HER Tafel slope being only 77 mV dec^{-1} (OER Tafel slope of 104.6 mV dec^{-1}). In both alkaline and seawater environments, the NiSe@$CoSe_2$ electrocatalyst exhibits excellent HER and OER performance. When employed in water splitting, the required voltage for water electrolysis is 1.91 V at 50 mA cm^{-2} (1.76 V at 30 mA cm^{-2} for seawater), and the catalyst demonstrates outstanding cyclic stability. Based on these results, NiSe@$CoSe_2$ shows great promise as an efficient bifunctional electrocatalyst for water electrolysis-based hydrogen production.

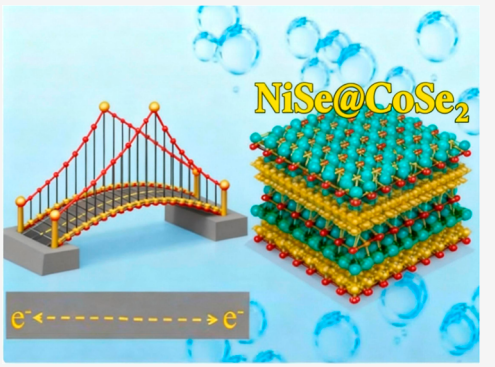

1. INTRODUCTION

With the continuous depletion of fossil fuels and the changing global energy landscape, the development, utilization, and storage of renewable energy sources have become urgent.[1−3] Both hydrogen and oxygen can store significant amounts of energy in the form of chemical bonds. Among them, hydrogen exhibits superior thermal efficiency and excellent sustainability.[4−6] At present, water electrolysis is regarded as one of the most promising methods for producing high-purity hydrogen and oxygen. However, the four-electron transfer kinetics of the oxygen evolution reaction (OER) are relatively slow, becoming the major bottleneck in the development of water electrolysis.[7,8] Therefore, designing and fabricating efficient bifunctional electrocatalysts is of great significance. Precious metal catalysts, such as those based on ruthenium (Ru) and platinum (Pt), are well-known for their excellent catalytic performance in both the hydrogen evolution reaction (HER) and OER.[9−11] However, their high cost and scarcity limit their large-scale application. To address these issues, the development of efficient bifunctional electrocatalysts is crucial.

Nickel-based compounds, with their low cost, nontoxicity, abundant resources, and the alkaline OER catalytic activity of Ni-based oxides, have attracted significant attention from researchers.[12−14] Among them, NiO is the primary subject of investigation within Ni-based oxides. Fominykh et al.[15] synthesized NiO nanoparticles via a hydrothermal method with an OER overpotential of 320 mV to achieve a current density of 10 mA cm^{-2}.[16] However, NiO suffers from low cyclic stability and poor conductivity, which prevents it from being widely used as a bifunctional electrocatalyst. Elakkiya et al. synthesized flower-like nanostructured $NiCo_2O_4$ using a simple method. It shows the OER and HER overpotentials of 360 mV and 370 mV at 10 mA cm^{-2}, respectively.[17] Although nickel-based compounds are considered ideal due to their excellent electrochemical properties, their inherent semiconducting nature increases the resistance to charge transfer, leading to reduced energy efficiency.[18] As a result, various strategies have been explored to enhance the water-splitting performance of these catalysts. Among these strategies, constructing heterogeneous structures is regarded as one of the most effective approaches.[19−21] This method leverages the synergistic effects between different materials and the interfacial effects of different components to improve the electrocatalytic performance.[22] Furthermore, transition metal

Received: September 14, 2025
Revised: December 21, 2025
Accepted: December 22, 2025
Published: December 26, 2025

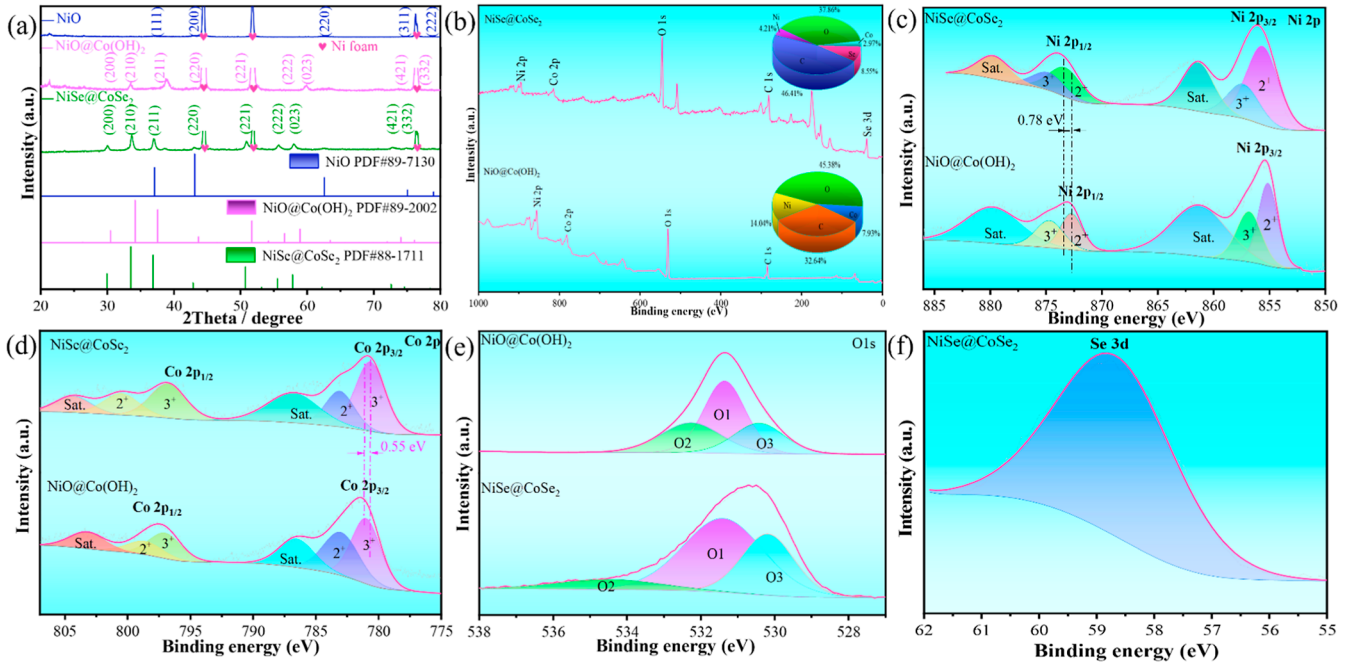

Figure 1. Structural characterization of the electrocatalytic samples. (a) XRD Pattern, (b) XPS full Spectrum and elemental composition, (c) Ni 2p, (d) Co 2p, (e) O 1s, (f) Se 3d.

selenides ($NiSe_2/CoSe_2$) have attracted widespread attention due to their strong electronegativity and fast charge transfer characteristics.[23] It facilitate gas separation and accelerate reaction rates during catalytic processes, thereby enhancing electrocatalytic performance.

In this study, we synthesized a $NiSe@CoSe_2$ electrocatalyst by hydrothermal method, doping selenium (Se) onto a nickel substrate and coating it with cobalt selenide. The semimetallic nature of Se and its compounds provide excellent conductivity, effectively addressing the charge transfer resistance issue in Ni-based compounds. The resulting $NiSe@CoSe_2$ electrocatalyst exhibits an HER overpotential of only −153.7 mV at 10 mA cm^{-2} in 1 M KOH (OER overpotential: 242.3 mV at 10 mA cm^{-2}) with a Tafel slope of 140.1 mV dec^{-1} (OER Tafel slope: 120.4 mV dec^{-1}) and excellent cyclic stability for 13 h. In seawater, at a current density of 10 mA cm^{-2}, the HER overpotential is −170.7 mV (OER overpotential: 156.5 mV at 30 mA cm^{-2}), with the HER Tafel slope being just 77 mV dec^{-1} (OER Tafel slope: 104.6 mV dec^{-1}). When used for full water splitting, the water splitting voltage is 1.91 V at 50 mA cm^{-2} (1.76 V in seawater at 30 mA cm^{-2}), and the catalyst also demonstrates outstanding cyclic stability. These exceptional properties make $NiSe@CoSe_2$ a highly efficient bifunctional electrocatalyst for water electrolysis.

2. EXPERIMENTAL SECTION

2.1. Synthesis of NiO. The nickel foam (4 cm × 5 cm) was treated in hydrochloric acid and ultrapure water for 30 min to remove surface oxides, and then dried in a vacuum oven at 60 °C for 15 min. The NiO sample was prepared via a hydrothermal method. The preparation process is as follows: 3 mM $Ni(NO_3)_2$, 6 mM $Co(NH_2)_2$, and 4 mM NH_4F were sequentially added to 60 mL of deionized water and stirred for 30 min using a magnetic stirrer until a homogeneous green solution was obtained. The solution was then poured into a reaction vessel, and the treated nickel foam was inserted into the solution. The reaction vessel was sealed tightly and placed in a vacuum oven at 120 °C for 6 h. After the reaction, the nickel foam was removed and rinsed with deionized water. It was then placed in a furnace for annealing at 350 °C for 2 h. After annealing, the sample was removed and labeled as the NiO sample.

2.2. Synthesis of $NiO@Co(OH)_2$. Two mM of $Co(NO_3)_2{\cdot}6H_2O$, 10 mM of $Co(NH_2)_2$, and 6 mM of NH_4F, and sequentially add them into 60 mL of deionized water. Stir the mixture for 30 min using a magnetic stirrer until the solution becomes a homogeneous pink color. The solution is then transferred into a reaction vessel, and the prepared NiO-coated nickel foam is inserted. After sealing the vessel, place it in a vacuum oven at 120 °C for 4 h. After the reaction, remove the nickel foam and rinse it with deionized water. The resulting sample is labeled as $NiO@Co(OH)_2$.

2.3. Synthesis of $NiSe@CoSe_2$. 0.5 g of Se powder and 5 g of NaOH, then dissolve the reagents in 60 mL of deionized water and stir for 30 min. Afterward, transfer the solution into a reaction vessel and insert the $NiO@Co(OH)_2$-coated nickel foam. Seal the vessel and place it in a vacuum oven at 180 °C for 16 h. After the reaction, remove the nickel foam and rinse it with deionized water. The resulting sample is labeled as $NiSe@CoSe_2$.

2.4. Materials Characterization. Scanning electron microscopy (SEM) was conducted using a Hitachi S-4800 microscope operating at 10 kV. X-ray diffraction (XRD) patterns were recorded on a D8 ADVANCE powder diffractometer (Bruker, Germany). X-ray photoelectron spectroscopy (XPS) analysis was performed on an ESCALAB 250Xi system with a power setting of 120 W.

2.5. Electrochemical Measurements. Electrochemical measurements were conducted at room temperature using a CH Instruments CHI760E electrochemical workstation with a three-electrode setup. The HER and OER tests were conducted in a three-electrode system, with the as-prepared electrocatalyst serving as the working electrode, Hg/AgO as the reference electrode, and a platinum sheet as the counter electrode for both HER and OER. The electrolyte used was 1.0 M KOH solution (pH = 13.7) and seawater. Electrochemical impedance spectroscopy (EIS) measurements were performed under an AC voltage with an amplitude of 5 mV and a frequency range of 0.01 Hz to 100 kHz. In addition, overall water splitting performance was tested in a two-electrode system, with the as-prepared electrocatalyst acting as both the working and counter electrodes, and a scan rate of 5 mV s^{-1}.

https://doi.org/10.1021/acs.energyfuels.5c04836
Energy Fuels 2026, 40, 721−729

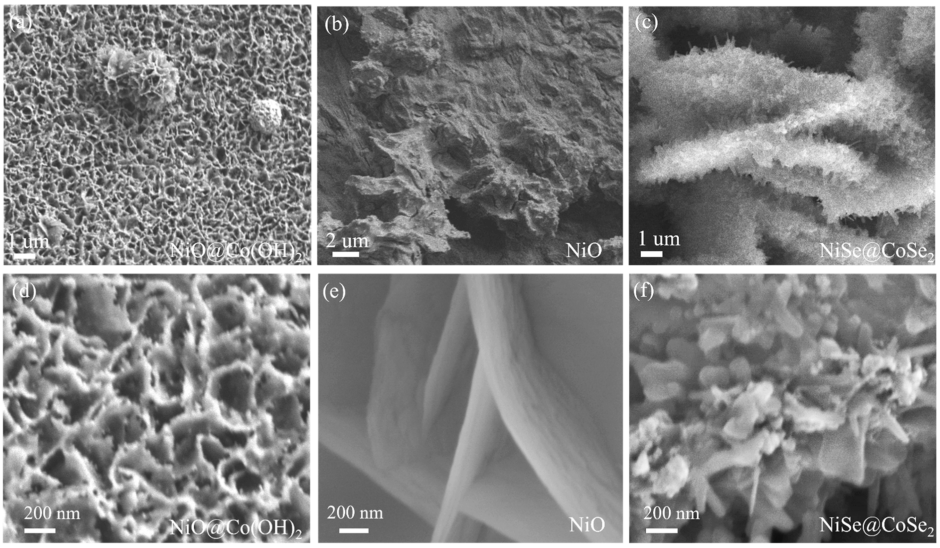

Figure 2. Structural characterization of the electrocatalytic samples. (a,b) NiO@$Co(OH)_2$ and NiO sample (c,d) NiSe@$CoSe_2$ and NiO@$Co(OH)_2$ sample (e,f) NiO and NiSe@$CoSe_2$ sample.

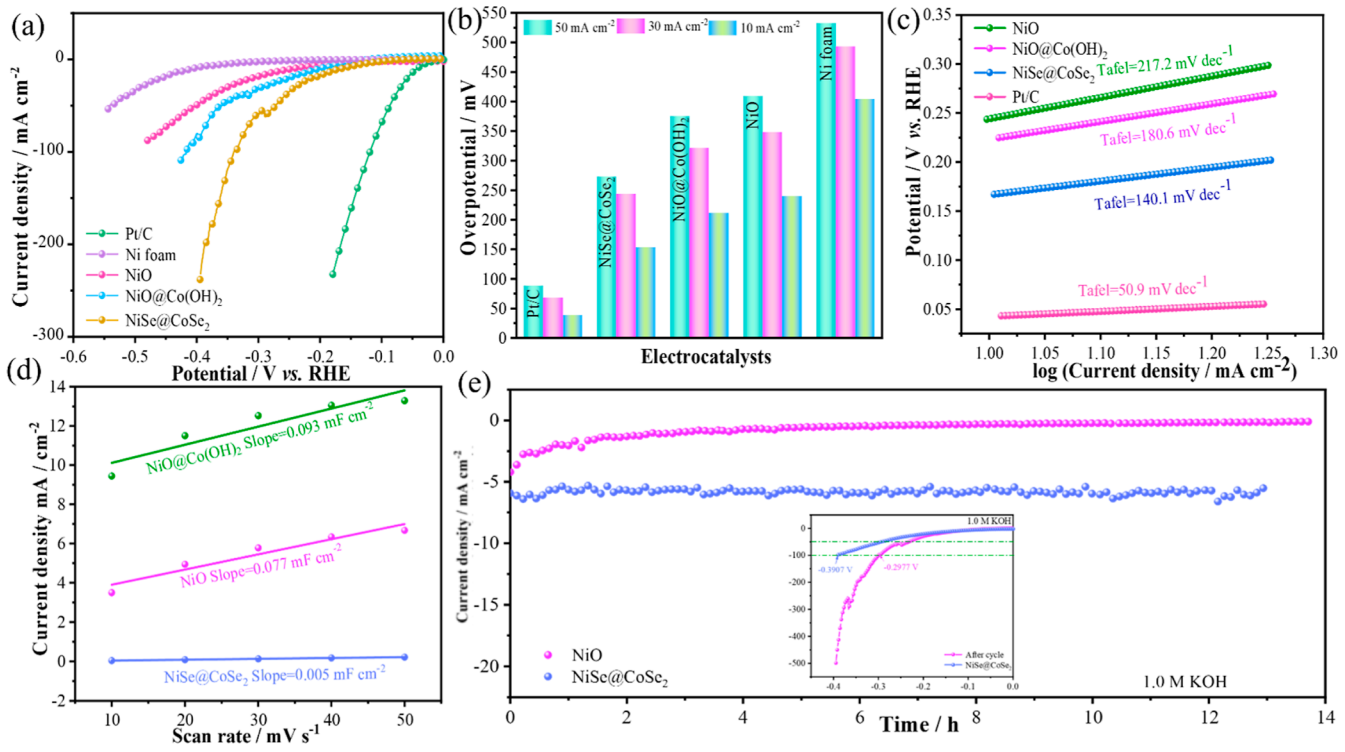

Figure 3. HER performance of each catalyst in alkaline electrolyte. (a) LSV curve of alkaline solution (b) overpotential of each catalyst (c) Tafel (d) C_{dl} diagram (e) cycle stability.

3. RESULTS AND DISCUSSION

To determine the phase structure and crystallinity of the synthesized catalysts, X-ray diffraction (XRD) was employed for material characterization. As shown in Figure 1a, the diffraction patterns of NiO (PDF#89-7130), NiO@$Co(OH)_2$ (PDF#89-2002), and NiSe@$CoSe_2$ (PDF#88-1711) catalysts are represented by blue, pink, and green, respectively. The three prominent peaks marked with red correspond to the characteristic peaks of nickel foam. The peaks at 18.5°, 21.5°, 31.3°, 37.5°, and 39.5° correspond to the (111), (200), (220), (311), and (222) crystal planes of NiO. The peaks at 15.2°, 17.1°, 18.8°, 21.8°, 23.2°, 27.1°, 28.3°, 37°, and 38.1° correspond to the (200), (210), (211), (220), (221), (222), (023), (421), and (332) crystal planes of NiO@$Co(OH)_2$. The peaks at 15°, 16.8°, 18.4°, 21.4°, 22.8°, 26.6°, 27.8°, 36.3°, and 37.3° correspond to the (200), (210), (211), (220), (221), (222), (023), (421), and (332) crystal planes of NiSe@$CoSe_2$. These diffraction peaks indicate that all materials exhibit excellent crystallinity and reveal that both NiO@$Co(OH)_2$ and NiSe@$CoSe_2$ crystals have complex cubic structures, confirming the successful synthesis of the samples with no significant structural distortion during preparation.

To further analyze the elemental composition and oxidation states of the synthesized samples, X-ray photoelectron

https://doi.org/10.1021/acs.energyfuels.5c04836
Energy Fuels 2026, 40, 721−729

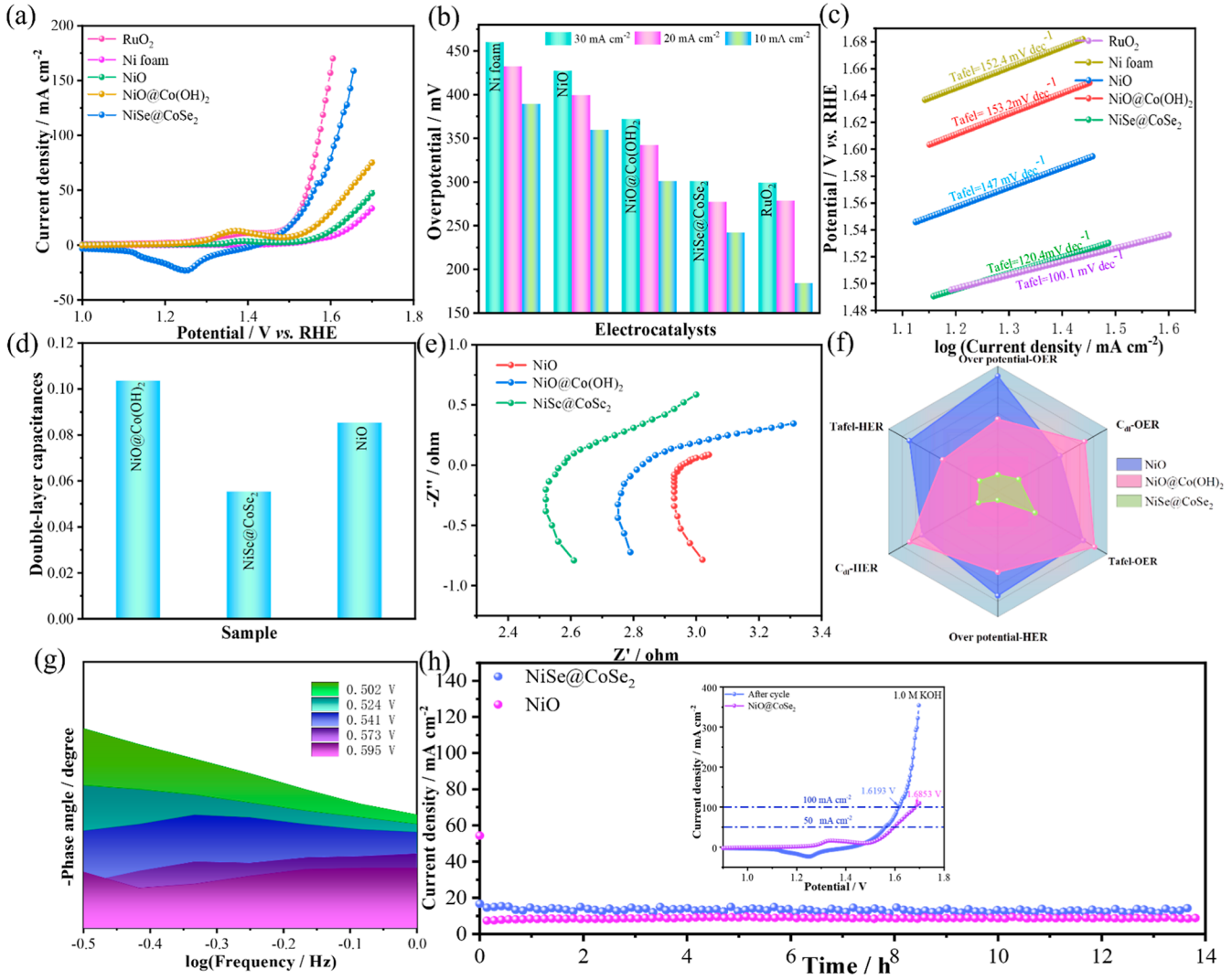

Figure 4. OER performance of each catalyst in alkaline electrolyte. (a) LSV curve of alkaline solution (b) overpotential (c) Tafel (d) C_{dl} (e) EIS (f) radar diagram (g) bode diagram (h) cycle stability.

spectroscopy (XPS) was conducted, as shown in Figure 1b–f. In Figure 1b, the NiSe@$CoSe_2$ sample contains the elements Ni, Co, O, C, and Se, whereas the NiO@$Co(OH)_2$ sample contains Ni, Co, O, and C. The elemental composition pie chart reveals that the Se content is 8.55%, indicating successful incorporation of selenium. In Figure 1c, the 873.4 and 875.1 eV peaks for the NiSe@$CoSe_2$ sample correspond to Ni^{2+} and Ni^{3+}, respectively, with a satellite peak observed at 879.9 eV.[24,25] Compared to the NiO@$Co(OH)_2$ sample, a shift of 0.78 eV to higher energies is observed, suggesting that the incorporation of Se enhances the electronic conductivity, facilitating the adsorption of H^+ and OH^- ions.[26] In Figure 1d, the 780.7 and 783.1 eV peaks for the NiSe@$CoSe_2$ sample correspond to Co^{3+} and Co^{2+}, respectively, with a satellite peak at 786.8 eV. Compared to the NiO@$Co(OH)_2$ sample, a shift of 0.55 eV to lower energies is observed.[27] In Figure 1e, the O 1s peak fitting reveals three characteristic peaks: the peak at 530.2 eV corresponds to metal–oxygen bonds, the peak at 531.5 eV corresponds to hydroxyl oxygen, and the peak at 534.6 eV is associated with adsorbed water.[28−30] Compared to the NiO@$Co(OH)_2$ sample, the peak associated with adsorbed water in the NiSe@$CoSe_2$ sample shifts significantly to higher energies, suggesting that the incorporation of selenium enhances the sample's attraction to water, thereby improving its catalytic performance. In Figure 1f, the peak at 58.8 eV corresponds to the Se 3d orbital.[31]

The morphology and structure of the electrocatalyst samples were characterized by scanning electron microscopy (SEM). As shown in Figure 2a-f, at low magnification (1 μm), the NiO catalyst exhibits an irregular shape, while at high magnification (200 nm), nanosheet structures are observed. This suggests that the NiO catalyst has a relatively small specific surface area and fewer exposed active sites. At low magnification (1 μm), the NiO@$Co(OH)_2$ catalyst shows several micrometer-sized nanospheres on the outer layer, with interlaced nanosheets beneath, indicating that the doping of cobalt has altered the structure of the material, providing more active sites. These active sites enhance the reaction rate, making the NiO@$Co(OH)_2$ catalyst exhibit better catalytic performance than the NiO catalyst. The NiSe@$CoSe_2$ catalyst shows a surface covered with numerous nanosheets, which are irregularly interlaced, improving the material's catalytic activity. This leads to faster charge transfer and kinetics, further enhancing the reaction rate.

To investigate the electrocatalytic activity of the prepared samples, the HER performance of the catalysts was first

https://doi.org/10.1021/acs.energyfuels.5c04836
Energy Fuels 2026, 40, 721−729

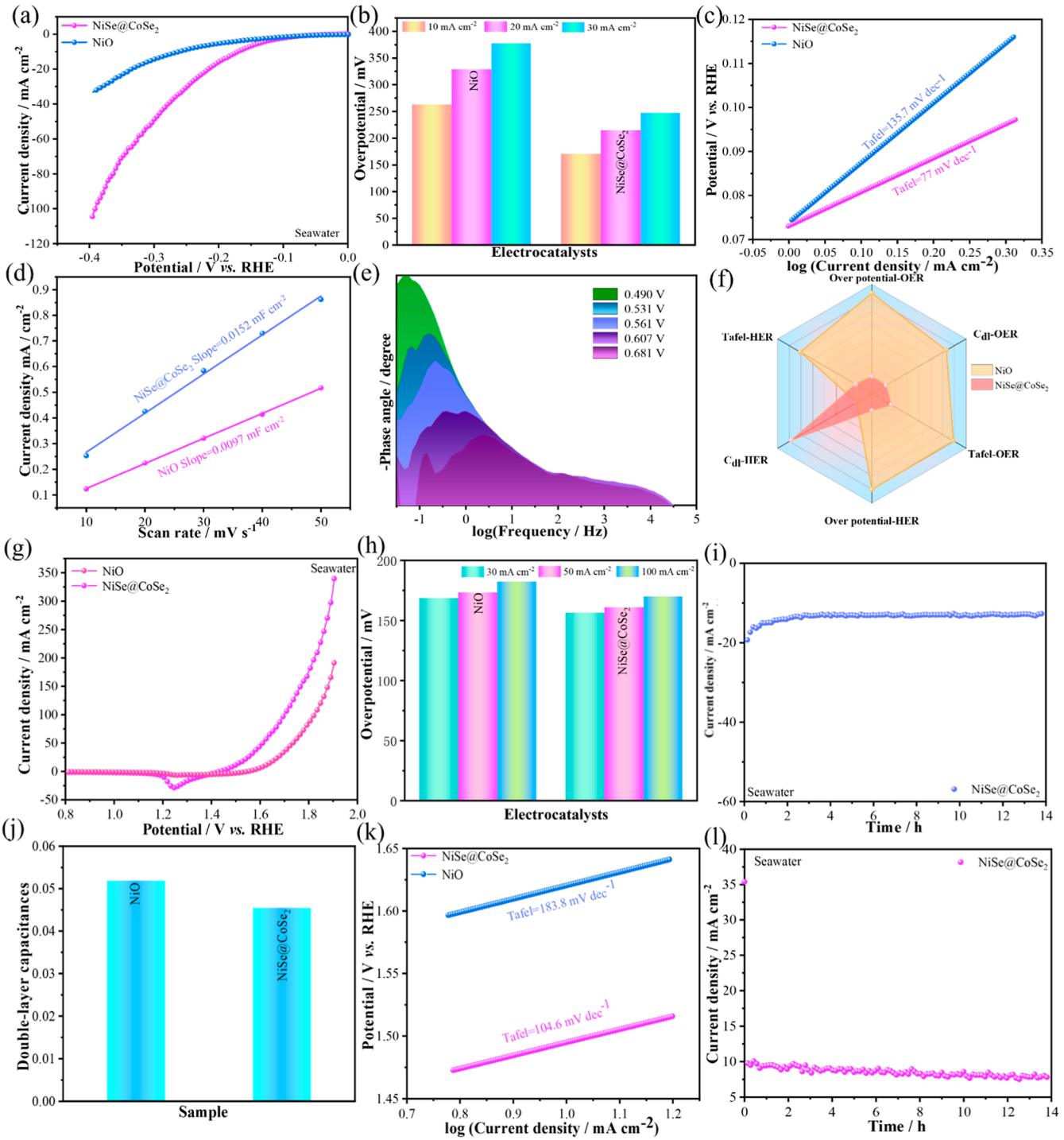

Figure 5. (a) LSV curve of HER seawater solution (b) overpotential of HER catalyst (c) Tafel (d) C_{dl} (e) bode diagram (f) radar (g) LSV curve of OER seawater solution (h) overpotential of OER catalyst (i) HER cycle (j) C_{dl} (k) Tafel (l) OER cycling.

evaluated in a 1.0 M KOH electrolyte. High overpotentials would hinder the widespread application of the samples in hydrogen evolution reactions. Figure 3a presents the LSV curves of all materials at a scan rate of 5 mV s^{-1} in 1.0 M KOH. The precious metal Pt/C catalyst exhibits an overpotential of −38.4 mV at 10 mA cm^{-2} and −88.4 mV at 50 mA cm^{-2}. The $NiSe@CoSe_2$ sample shows an overpotential of −153.7 mV at a current density of 10 mA cm^{-2}, and −272.7 mV at 50 mA cm^{-2}, which is significantly lower than the overpotentials of NiO (−239.7 mV at 10 mA cm^{-2} and −409.7 mV at 50 mA cm^{-2}) and $NiO@Co(OH)_2$ (−211.7 mV at 10 mA cm^{-2} and −375.7 mV at 50 mA cm^{-2}). These results indicate that the catalytic performance improves after selenization. The nickel foam substrate shows overpotentials of −404.7 mV at 10 mA cm^{-2} and −532.7 mV at 50 mA cm^{-2}, suggesting that its impact on the catalytic performance is negligible. To further study the reaction kinetics of the catalysts, Tafel slopes were calculated from the LSV curves, as shown in Figure 3c. The Tafel slope of the $NiSe@CoSe_2$ catalyst is 140.1 mV dec^{-1}, lower than that of $NiO@Co(OH)_2$ (180.6 mV dec^{-1}) and

https://doi.org/10.1021/acs.energyfuels.5c04836
Energy Fuels 2026, 40, 721−729

NiO (217.2 mV dec^{-1}). This demonstrates that the catalyst performance improves during the doping process, with the NiSe@$CoSe_2$ sample exhibiting fast charge transfer and kinetic reaction rates, consistent with the conclusions drawn from the LSV curves. In the electrocatalytic hydrogen evolution reaction, the catalytic activity of the catalyst is determined by its electrochemical active surface area (ECSA), which is positively correlated with its electrochemical double-layer capacitance (C_{dl}). Thus, by studying the C_{dl} of the sample catalysts, the intrinsic activity of the catalysts can be inferred. As shown in Figure 3d, the C_{dl} value of NiO is 0.077 mF cm^{-2}, and that of NiO@$Co(OH)_2$ is 0.093 mF cm^{-2}, indicating that selenization altered the structure of NiO and increased the reaction sites, thereby enlarging the surface area in contact with the electrolyte. More reaction sites correspond to higher electrocatalytic activity. The C_{dl} value of NiSe@$CoSe_2$ is 0.005 mF cm^{-2}, smaller than that of NiO@$Co(OH)_2$, suggesting that after selenization, the catalyst sample provides fewer reaction sites but has higher intrinsic activity. Electrochemical stability is another important evaluation index for catalysts. To assess the durability of the samples, chronopotentiometry was performed for 13 h in a 1.0 M KOH electrolyte. As shown in Figure 3e, the LSV curves before and after cycling of the NiSe@$CoSe_2$ sample reveal that after cycling, the overpotential of the sample (−0.2977 V) is lower than before cycling (−0.3907 V), indicating that the performance improved after long-term cycling. Overall, the NiSe@$CoSe_2$ sample demonstrated excellent HER performance, as well as good stability and long-term durability.

To evaluate the OER performance of the catalysts, a three-electrode system was used in the 1.0 M KOH electrolyte. Figure 4a shows the LSV curves of all materials at a scan rate of 5 mV s^{-1}. The RuO_2 catalyst exhibits overpotentials of 184.3 mV at 10 mA cm^{-2} and 299.3 mV at 30 mA cm^{-2}. The NiSe@$CoSe_2$ sample shows an overpotential of 242.3 mV at 10 mA cm^{-2} and 301.3 mV at 30 mA cm^{-2}, which are significantly lower than those of the NiO catalyst (359.3 mV at 10 mA cm^{-2} and 427.3 mV at 30 mA cm^{-2}) and NiO@$Co(OH)_2$ catalyst (301.3 mV at 10 mA cm^{-2} and 372.3 mV at 30 mA cm^{-2}). The nickel foam substrate shows overpotentials of 389.3 mV at 10 mA cm^{-2} and 460.3 mV at 30 mA cm^{-2}, indicating its negligible effect on oxygen evolution catalysis. The Tafel slopes of the catalysts, calculated from the LSV curves, are shown in Figure 4c. The Tafel slope of NiSe@$CoSe_2$ is 120.4 mV dec^{-1}, lower than those of NiO@$Co(OH)_2$ (153.2 mV dec^{-1}) and NiO (147 mV dec^{-1}), indicating fast charge transfer and kinetic reaction rates, consistent with the LSV results. As shown in Figure 4d, the C_{dl} values of NiO (0.0855 mF cm^{-2}) and NiO@$Co(OH)_2$ (0.1036 mF cm^{-2}) are larger than that of NiO, indicating that selenization increases the reaction sites. Further study of the charge transfer ability of the catalysts in alkaline media is shown in the electrochemical impedance spectroscopy (EIS) curves in Figure 4e. The intrinsic resistance values are NiO (2.96 Ω) > NiO@$Co(OH)_2$ (2.83 Ω) > NiSe@$CoSe_2$ (2.58 Ω), indicating that the composite enhances the intrinsic conductivity of the catalyst, increasing effective charge transfer and thereby improving the electrocatalytic performance of NiSe@$CoSe_2$. The Bode plot in Figure 4g reveals charge transfer signals at different characteristic frequencies, with the catalyst−electrolyte interface charge transfer occurring in the low-frequency range. The highest peak decreases with increasing potential, indicating enhanced catalytic activity. As shown in Figure 4h, after long-term cycling, the overpotential of the NiSe@$CoSe_2$ sample at 100 mA cm^{-2} (1.6193 V) is lower than before cycling (1.6853 V), suggesting improved performance after extended cycling. Overall, the NiSe@$CoSe_2$ sample also exhibited excellent OER performance, as well as good stability and long-term durability. The radar chart summarizes the HER overpotential, OER overpotential, HER Tafel slope, OER Tafel slope, C_{dl} for HER, and C_{dl} for OER, showing that NiSe@$CoSe_2$ outperforms all other samples, demonstrating its excellent catalytic performance in alkaline electrolyte.

The corresponding HER performance of the catalysts in seawater was also evaluated. Figure 5a shows the linear sweep voltammetry (LSV) curves of all materials at a scan rate of 5 mV s^{-1} in Seawater electrolyte. The NiSe@$CoSe_2$ sample exhibited an overpotential of −170.7 mV at a current density of 10 mA cm^{-2} (Figure 5b), and its overpotential remained low at −247.7 mV at 30 mA cm^{-2}. This overpotential is significantly lower than that of the NiO catalyst, which showed −262.7 mV at 10 mA cm^{-2} and −377.7 mV at 30 mA cm^{-2}. Further investigation into the reaction kinetics of the samples was carried out by fitting the LSV curves to extract the corresponding Tafel slopes, as shown in Figure 5c. The Tafel slope of the NiSe@$CoSe_2$ catalyst was 77 mV dec^{-1}, lower than that of NiO (135.7 mV dec^{-1}). These results suggest that the performance of the catalyst improved after selenium doping, with NiSe@$CoSe_2$ demonstrating rapid charge transfer and kinetic reaction rates in Seawater, consistent with the conclusions obtained from the linear sweep voltammetry (LSV) curves. As shown in Figure 5d, the C_{dI} value of the NiO sample was 0.0097 mF cm^{-2}, while that of NiO@$CoSe_2$ was 0.0152 mF cm^{-2}. The higher C_{dI} value of NiO@$CoSe_2$ indicates an increased number of active sites after selenium doping, which enhanced the reaction rate and improved the electrocatalytic activity of the NiO@$CoSe_2$ sample. The Bode plots in Figure 5e show two distinct regions: a low-frequency region on the left and a high-frequency region on the right. As the voltage increases, the highest peak rapidly declines, indicating faster charge transfer between the catalyst and the electrolyte.[32] it demonstrates that the NiSe@$CoSe_2$ sample exhibits better catalytic performance in seawater electrolyte than in alkaline electrolyte. The radar chart in Figure 5f presents the integrated performance across six aspects: HER overpotential, OER overpotential, HER-Tafel slope, OER-Tafel slope, C_{dI}-HER, and C_{dI}-OER. The comprehensive analysis reveals that the NiSe@$CoSe_2$ sample has the best overall performance, indicating its excellent catalytic activity in Seawater electrolyte.

Similarly, to further investigate the electrocatalytic activity of the prepared samples, the OER performance of the catalysts in Seawater was assessed. Figure 5g shows the LSV curves of all materials at a scan rate of 5 mV s^{-1} in Seawater electrolyte. The NiSe@$CoSe_2$ sample exhibited an overpotential of 156.5 mV at a current density of 30 mA cm^{-2}, and 170 mV at 100 mA cm^{-2} (Figure 5h). These overpotentials are lower than those of the NiO catalyst, which had an overpotential of 168.7 mV at 30 mA cm^{-2} and 182.3 mV at 100 mA cm^{-2}. As shown in Figure 5i, the NiSe@$CoSe_2$ sample maintained good stability after 13 h of cycling in Seawater electrolyte. Figure 5j shows that the C_{dI} value of the NiO sample was 0.0519 mF cm^{-2}, which is higher than the C_{dI} value of NiSe@$CoSe_2$ (0.0455 mF cm^{-2}), indicating an enhancement in the intrinsic activity of the catalyst itself. To further investigate the reaction kinetics of the catalyst in Seawater electrolyte, the Tafel slope

https://doi.org/10.1021/acs.energyfuels.5c04836
Energy Fuels 2026, 40, 721−729

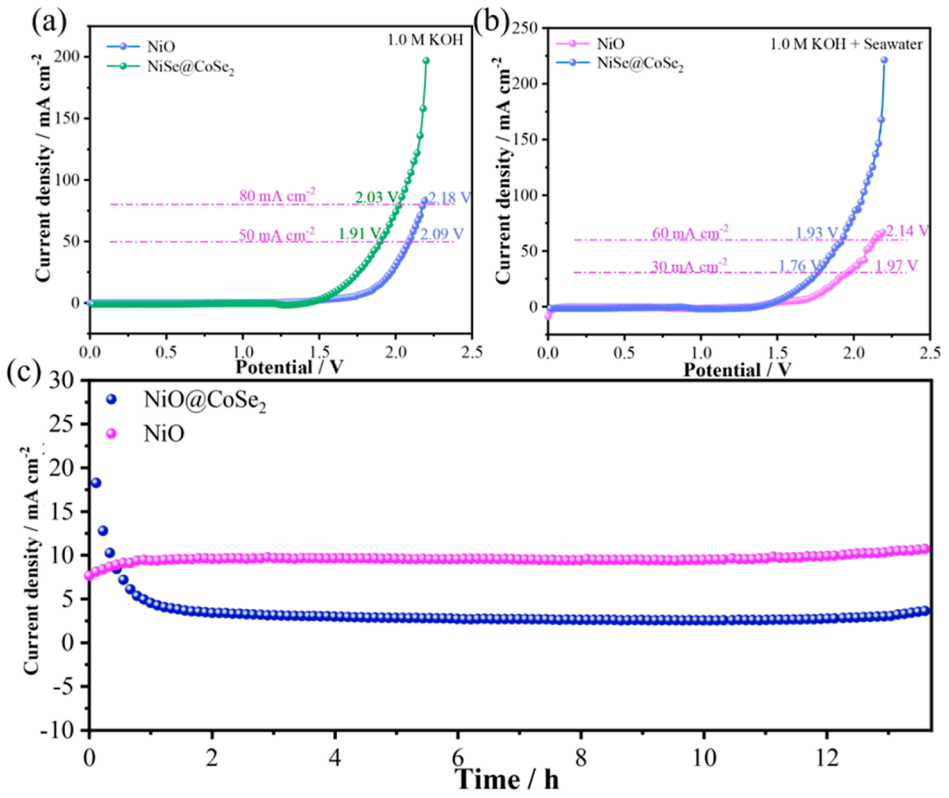

Figure 6. (a) LSV curve of 1.0 M KOH solution (b) LSV curve of 1.0 M KOH seawater solution (c) cycle stability.

was calculated from the LSV curve fitting, as shown in Figure 5k. The Tafel slope of the NiSe@$CoSe_2$ catalyst was 104.6 mV dec^{-1}, lower than that of NiO (183.8 mV dec^{-1}). Figure 5l shows that the NiSe@$CoSe_2$ sample exhibited good stability after 13 h of cycling in Seawater electrolyte.

The above studies demonstrate that the NiSe@$CoSe_2$ catalyst maintains excellent HER and OER performance in both 1.0 M KOH and Seawater electrolytes. Therefore, the NiSe@$CoSe_2$ catalyst can serve as a bifunctional electrocatalyst for water splitting. Figure 6a shows the linear sweep voltammetry (LSV) curves of the catalyst in 1.0 M KOH electrolyte at a scan rate of 5 mV s^{-1}, with the catalyst acting as both the cathode and anode. At a current density of 50 mA cm^{-2}, the potential of the NiSe@$CoSe_2$ catalyst was 1.91 V, lower than the NiO catalyst's potential of 2.09 V. At a current density of 80 mA cm^{-2}, the potential of NiSe@$CoSe_2$ was 2.03 V, again lower than that of NiO, which was 2.18 V. This indicates that the NiSe@$CoSe_2$ catalyst requires a lower voltage to achieve a certain current density, demonstrating its high electrocatalytic activity and relatively low energy loss during water electrolysis. Figure 6b presents the LSV curves for Seawater electrolyte at a scan rate of 5 mV s^{-1}. At a current density of 30 mA cm^{-2}, the potential of NiSe@$CoSe_2$ was 1.76 V, lower than the NiO catalyst's potential of 1.97 V. At 60 mA cm^{-2}, the potential of NiSe@$CoSe_2$ was 1.93 V, lower than that of NiO, which was 2.14 V. In Seawater electrolyte, the NiSe@$CoSe_2$ catalyst similarly requires a lower voltage to achieve a specific current density, indicating that the catalyst retains high electrochemical activity and low energy loss even in Seawater. Electrochemical stability is another key evaluation criterion for catalysts. A chronoamperometric test was conducted for 13 h with the catalyst acting as both the anode and cathode in 1.0 M KOH electrolyte. As shown in Figure 6c, the NiSe@$CoSe_2$ catalyst exhibited better stability than the NiO catalyst, with no significant current decay.

4. CONCLUSION

We have successfully prepared NiSe@$CoSe_2$, NiO@$Co(OH)_2$, and NiO catalysts via the hydrothermal method. The catalysts' morphology and structure were analyzed, and their electrocatalytic performance under various conditions was evaluated. For the HER performance in alkaline electrolyte, the NiSe@$CoSe_2$ sample exhibited an overpotential of −153.7 mV at a current density of 10 mA cm^{-2} and −272.7 mV at 50 mA cm^{-2}. The OER overpotentials were 242.3 mV at 10 mA cm^{-2} and 301.3 mV at 50 mA cm^{-2}, with a Tafel slope of 140.1 mV dec^{-1} (for OER, the Tafel slope was 120.4 mV dec^{-1}). In Seawater electrolyte, the NiSe@$CoSe_2$ sample exhibited an overpotential of −170.7 mV at 10 mA cm^{-2} and −247.7 mV at 30 mA cm^{-2}, with the OER overpotentials being 156.5 mV at 30 mA cm^{-2} and 170 mV at 100 mA cm^{-2}. The Tafel slope for HER was 77 mV dec^{-1}, and for OER, it was 104.6 mV dec^{-1}. As a bifunctional electrocatalyst, the voltage for water splitting in alkaline electrolyte was 1.91 V at 50 mA cm^{-2} (1.76 V in Seawater electrolyte at 30 mA cm^{-2}), with excellent cyclic stability. This study offers a novel approach for the rational design and preparation of efficient bifunctional electrocatalysts, laying the foundation for the development of more efficient electrocatalytic materials for alkaline and seawater electrolytes.

AUTHOR INFORMATION

Corresponding Author

Lihua Miao − *School of Medical Information Engineering, Shenyang Medical College, Shenyang, Liaoning 110034, P. R. China;* orcid.org/0000-0001-8244-5211;
Email: miaolihua@163.com

https://doi.org/10.1021/acs.energyfuels.5c04836
Energy Fuels 2026, 40, 721−729

Authors

Yijia Cheng − *School of Medical Information Engineering, Shenyang Medical College, Shenyang, Liaoning 110034, P. R. China*

Lili Sui − *School of Medical Information Engineering, Shenyang Medical College, Shenyang, Liaoning 110034, P. R. China*

Xingyan Guo − *School of Medical Information Engineering, Shenyang Medical College, Shenyang, Liaoning 110034, P. R. China*

Dan Yang − *School of Medical Information Engineering, Shenyang Medical College, Shenyang, Liaoning 110034, P. R. China*

Shuai Du − *School of Electronic Information Science and Technology, Liaoning University, Shenyang, Liaoning 110036, P. R. China*

Complete contact information is available at: https://pubs.acs.org/10.1021/acs.energyfuels.5c04836

Notes

The authors declare no competing financial interest.

■ ACKNOWLEDGMENTS

This project is supported by College Student Innovation and Entrepreneurship Project (S202410164017).

■ REFERENCES

(1) Megía, P. J.; Vizcaíno, A. J.; Calles, J. A.; Carrero, A. Hydrogen production technologies: From fossil fuels toward renewable sources. A mini review. *Energy Fuels* **2021**, *35* (20), 16403−16415.

(2) Brockway, P. E.; Owen, A.; Brand-Correa, L. I.; Hardt, L. Estimation of global final-stage energy-return-on-investment for fossil fuels with comparison to renewable energy sources. *Nat. Energy* **2019**, *4* (7), 612−621.

(3) Shindell, D.; Smith, C. J. Climate and air-quality benefits of a realistic phase-out of fossil fuels. *Nature* **2019**, *573* (7774), 408−411.

(4) Abdin, Z.; Zafaranloo, A.; Rafiee, A.; Mérida, W.; Lipiński, W.; Khalilpour, K. R. Hydrogen as an energy vector. *Renew. Sustain. Energy Rev.* **2020**, *120*, 109620.

(5) Li, R. Y.; Xu, S. L.; Ai, Z. Q.; Qi, J. G.; Wu, F. F.; Zhao, R. D.; Zhao, D. P. Interface engineering accelerated surface reconstruction for electrocatalytic water splitting and energy storage devices through hybrid structured $ZnCo_2O_4$@NiCo-LDH nanocomposites. *Int. J. Hydrogen Energy* **2024**, *91*, 867−876.

(6) Xu, S. L.; Zhao, R. D.; Li, R. Y.; Li, J.; Xiang, J.; Guo, F. Y.; Qi, J. G.; Liu, L.; Wu, F. F. Constructing high-performance supercapacitors and electrochemical water splitting electrode materials through core−shell structured Co_9S_8@$Ni(OH)_2$ nanosheets. *J. Mater. Chem. A* **2024**, *12*, 15950−15965.

(7) Ruocco, C.; Palma, V.; Ricca, A. Kinetics of oxidative steam reforming of ethanol over bimetallic catalysts supported on CeO_2−SiO_2. *Top. Catal.* **2019**, *62* (5−6), 467−476.

(8) Li, R. Y.; Shen, X. Y.; Li, J.; Zhao, D. P.; Zhao, R. D.; Wu, F. F. Enhanced electrochemical performance of NiCo-layered double hydroxides: Optimal synthesis conditions and supercapacitor applications. *Adv. Sustain. Syst.* **2025**, *9* (2), 2400753.

(9) Brauns, J.; Turek, T. Alkaline water electrolysis powered by renewable energy: A review. *Processes* **2020**, *8* (2), 248.

(10) Du, Z.; Yu, F.; Wang, J.; Li, J.; Wang, X.; Qian, A. Catalytic effects of graphene structures on Pt/graphene catalysts. *RSC Adv.* **2024**, *14* (31), 22486−22496.

(11) Wu, B.; Gong, S.; Lin, Y.; Li, T.; Chen, A.; Zhao, M.; Zhang, Q.; Chen, L. A unique NiOOH@FeOOH heteroarchitecture for enhanced oxygen evolution in saline water. *Adv. Mater.* **2022**, *34*, 2108619.

(12) Xiao, Q.; Wang, X.; Huang, S. Facile synthesis of $Ni(OH)_2$ nanowires on nickel foam via a one-step low-temperature hydrothermal route for non-enzymatic glucose sensors. *Mater. Lett.* **2017**, *198*, 19−22.

(13) Zhao, D. P.; Dai, M. Z.; Liu, H. Q.; Duan, Z. X.; Tan, X. J.; Wu, X. Bifunctional $ZnCo_2S_4$@$CoZn_{13}$ hybrid electrocatalysts for highly efficient overall water splitting. *J. Energy Chem.* **2022**, *69*, 292−300.

(14) Gong, S.; Du, Z.; Tang, Y.; Chen, J. Encapsulation of Ru nanoparticles within NaY zeolite for ammonia decomposition. *Int. J. Hydrogen Energy* **2024**, *88*, 142−150.

(15) Kannan, V.; Inamdar, A. I.; Pawar, S. M.; Kim, H.-S.; Park, H.-C.; Kim, H.; Im, H.; Chae, Y. S. Facile Route to NiO Nanostructured Electrode Grown by Oblique Angle Deposition Technique for Supercapacitors. *ACS Appl. Mater. Interfaces.* **2016**, *8*, 17220.

(16) Cui, D.; Zhao, R. D.; Dai, J. Q.; Xiang, J.; Wu, F. F. A hybrid $NiCo_2O_4$@$NiMoO_4$ structure for overall water splitting and excellent hybrid energy storage. *Dalton Trans.* **2020**, *49*, 9668−9676.

(17) Elakkiya, R.; Ramkumar, R.; Maduraiveeran, G. Flower-like nickel−cobalt oxide nanomaterials as bifunctional catalysts for electrochemical water splitting. *Mater. Res. Bull.* **2019**, *116*, 98−105.

(18) Wu, L.; Ning, M.; Xing, X.; Wang, Y.; Zhang, F.; Gao, G.; Song, S.; Wang, D.; Yuan, C.; Yu, L.; Bao, J.; Chen, S.; Ren, Z. Boosting oxygen evolution reaction of (Fe, Ni)OOH via defect engineering for anion exchange membrane water electrolysis under industrial conditions. *Adv. Mater.* **2023**, *35*, 2306097.

(19) Chen, Z.; Fei, B.; Hou, M.; Yan, X.; Chen, M.; Qing, H.; Wu, R. Ultrathin Prussian blue analogue nanosheet arrays with open bimetal centers for efficient overall water splitting. *Nano Energy* **2020**, *68*, 104371.

(20) Di, Y. F.; Xiang, J.; Bu, N.; Loy, S.; Yang, W. D.; Zhao, R. D.; Wu, F. F.; Sun, X. B.; Wu, Z. H. Sophisticated structural tuning of $NiMoO_4$@$MnCo_2O_4$ nanomaterials for high-performance hybrid capacitors. *Nanomaterials* **2022**, *12*, 1674.

(21) Wang, H.; Li, J.; Li, K.; Lin, Y.; Chen, J.; Gao, L.; Nicolosi, V.; Xiao, X.; Lee, J. M. Transition metal nitrides for electrochemical energy applications. *Chem. Soc. Rev.* **2021**, *50*, 1354−1390.

(22) Liu, L.; Mo, J.; Xu, J.; Liu, Y.; Yang, R.; Yang, X.; Ma, X.; Fu, W. Directional movement of electron induced by interfacial coupling in CuS@NiCo-LDHs for efficient alkaline oxygen evolution reaction. *Appl. Surf. Sci.* **2024**, *665*, 160311.

(23) Wang, X.; Wang, J.; Yang, Y.; Wu, Q.; Zhang, C.; Wang, J.; Xu, R.; Yang, L. Boosting the electrocatalytic activity of NiCoS by Zr doping as a promising electrocatalyst for oxygen evolution reaction. *Appl. Surf. Sci.* **2023**, *640*, 158361.

(24) Wang, X.; Wang, Z.; Jia, B.; Li, C.; Sun, S.; Hu, S. Concerted proton-coupled electron transfer promotes NiCoP nanowire arrays for efficient overall water splitting at industrial-level current density. *Chem. Eng. J.* **2024**, *479*, 147450.

(25) Zhong, X.; Zhang, L.; Tang, J.; Chai, J.; Xu, J.; Cao, L.; Yang, M.; Yang, M.; Kong, W.; Wang, S.; et al. Efficient coupling of a hierarchical V_2O_5@Ni_3S_2 hybrid nanoarray for pseudocapacitors and hydrogen production. *J. Mater. Chem. A* **2017**, *5* (34), 17954−17962.

(26) Yang, W. D.; Zhao, R. D.; Guo, F. Y.; Xiang, J.; Loy, S.; Liu, L.; Dai, J. Y.; Wu, F. F. Interface engineering of hybrid $ZnCo_{2O4}$@$Ni_{2.5}Mo_6S_{6.7}$ structures for flexible energy storage and alkaline water splitting. *Chem. Eng. J.* **2023**, *454*, 140458.

(27) Zhao, D. P.; Liu, X. Y.; Zhang, W. C.; Wu, X.; Cho, Y. R. Highly efficient and stable Mo−CoP_3@FeOOH electrocatalysts for alkaline seawater splitting. *Small Methods* **2024**, *8*, 2301474.

(28) Yang, W. D.; Xiang, J.; Zhao, R. D.; Loy, S.; Li, M. T.; Ma, D. M.; Li, J.; Wu, F. F. Nanoengineering of $ZnCo_2O_4$@$CoMoO_4$ heterogeneous structures for supercapacitor and water splitting applications. *Ceram. Int.* **2023**, *49* (3), 4422−4434.

(29) Zhao, D. P.; Dai, M. Z.; Liu, H. Q.; Duan, Z. X.; Tan, X. J.; Wu, X. Bifunctional $ZnCo_2S_4$ hybrid electrocatalysts for highly efficient overall water splitting. *J. Energy Chem.* **2022**, *69*, 292−300.

(30) Yan, J. G.; Chen, L. G.; Liang, X. Co_9S_8 nanowires@NiCo-LDH nanosheet arrays on nickel foam toward efficient overall water splitting. *Sci. Bull.* **2019**, *64*, 158−165.

(31) Wang, P.; Luo, Y. Z.; Zhang, G. X.; Chen, Z. S.; Ranganathan, H.; Sun, S. H.; Shi, Z. C. Interface engineering of $Ni_xS\gamma$@$MnO_xH\gamma$ nanorods to efficiently enhance overall water splitting activity and stability. *Nano-Micro Lett.* **2022**, *14*, 120.
(32) Liu, H. Q.; Zhao, D. P.; Dai, M. Z.; Zhu, X. F.; Qu, F. Y.; Umar, A.; Wu, X. PEDOT-decorated $CoNi_2S_4$ nanosheet electrodes as bifunctional electrocatalysts for enhanced electrocatalysis. *Chem. Eng. J.* **2022**, *428*, 131183.

https://doi.org/10.1021/acs.energyfuels.5c04836
Energy Fuels 2026, 40, 721−729